

FULL PAPER

Open Access



Cold proton nonresonant response to EMIC waves: MMS observations and a hybrid simulation

Huayue Chen^{1*} Xueyi Wang^{1*}, Lunjin Chen², Chih-Ping Wang³, Xiaolei Li¹, Yu Lin¹, Hong Zhao¹, Yoshiharu Omura⁴, Yi-Kai Hsieh⁴, Xinmin Li⁵, Levon A. Avanov⁶, Hanying Wei⁷ and Narges Ahmadi⁸

Abstract

Cold protons play an important role in the Earth's magnetosphere by modifying the dispersion relation of plasma waves. Their energy flux can be enhanced through a nonresonant response to electromagnetic ion cyclotron (EMIC) waves. This study combines Magnetospheric Multiscale (MMS) observations and a hybrid simulation to investigate cold proton dynamics during this nonresonant process. It is found that the energy flux of cold protons with kinetic energies below ~ 200 eV increases due to the bulk flow induced by EMIC waves, and this enhancement becomes stronger and extends to higher energies at higher magnetic latitudes. Despite the flux enhancement, the temperature and number density of cold protons remain constant. Moreover, we identify the formation mechanism of proton phase-bunching distribution in stationary gyrophase. During the nonresonant process, particles bunch in anti-phase with the wave magnetic fields, without exchanging energy with waves. In contrast, during the resonant process, particles bunch in anti-phase with the wave electric fields, facilitating energy transfer from particles to waves. We demonstrate that particle phase-bunching is a necessary but not sufficient condition for identifying resonant interactions with waves, and that the occurrence of energy transfer determines whether the response is nonresonant or resonant.

Keywords Cold proton flux enhancement, Electromagnetic ion cyclotron (EMIC) waves, Nonresonant response, Phase-bunching distribution

*Correspondence:

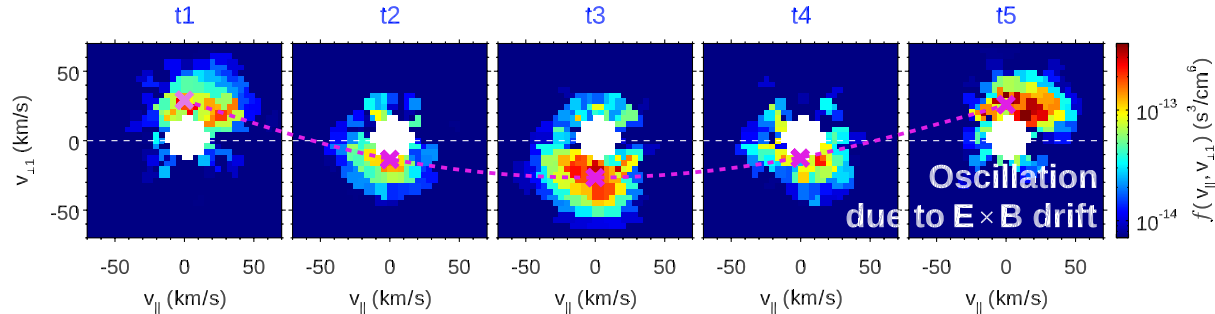
Huayue Chen
huayue_chen@foxmail.com
Xueyi Wang
wangxue@auburn.edu

Full list of author information is available at the end of the article

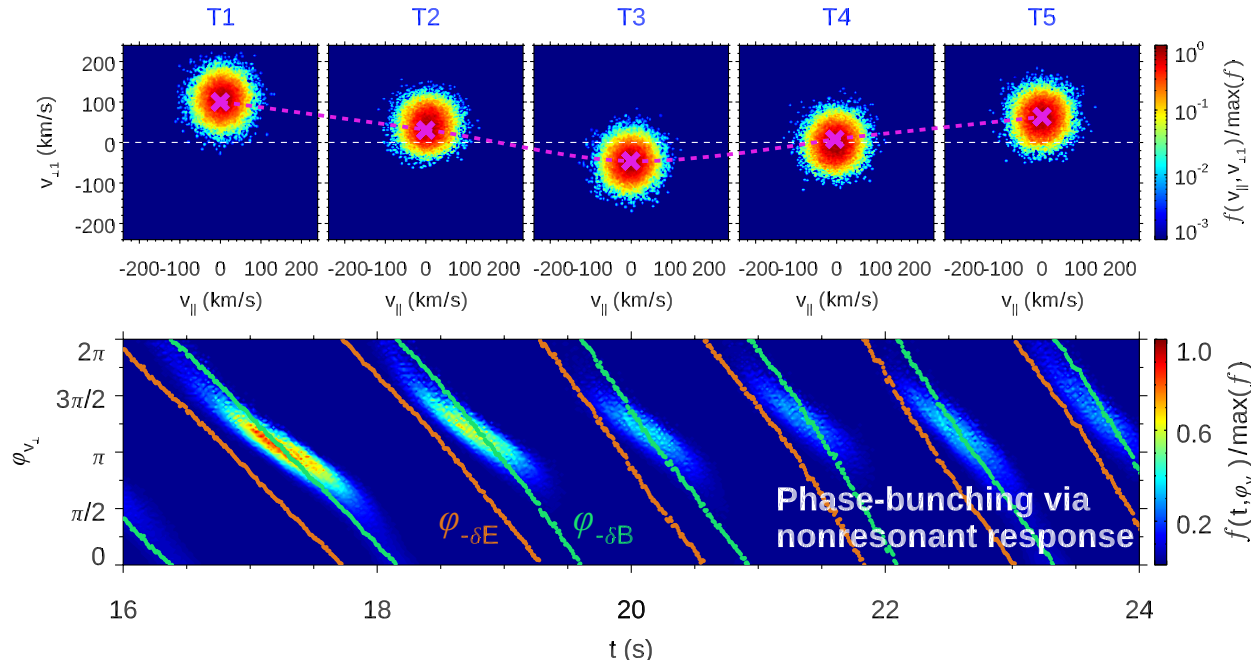
© The Author(s) 2026. **Open Access** This article is licensed under a Creative Commons Attribution 4.0 International License, which permits use, sharing, adaptation, distribution and reproduction in any medium or format, as long as you give appropriate credit to the original author(s) and the source, provide a link to the Creative Commons licence, and indicate if changes were made. The images or other third party material in this article are included in the article's Creative Commons licence, unless indicated otherwise in a credit line to the material. If material is not included in the article's Creative Commons licence and your intended use is not permitted by statutory regulation or exceeds the permitted use, you will need to obtain permission directly from the copyright holder. To view a copy of this licence, visit <http://creativecommons.org/licenses/by/4.0/>.

Graphical Abstract

MMS observations



Hybrid simulation



1 Introduction

Cold plasma in the Earth's magnetosphere, composed of ions and electrons with kinetic energies below a few hundred eV (Denton & Borovsky 2008; Gary et al. 2012; Delzanno et al., 2021), makes a major contribution to the total plasma density (Hultqvist 1971; Matsui et al. 1999; André et al. 2010). These populations mainly originate from the ionosphere and flow upward along magnetic field lines into the magnetosphere (Axford 1968; Hultqvist 1971; Engwall et al. 2009).

Cold plasma is crucial for wave excitation and propagation. Electromagnetic ion cyclotron (EMIC) waves can be guided by cold plasma density gradients, which maintain small wave normal angles and enhance path-integrated gain (Horne & Thorne 1994; Chen et al. 2009). This mechanism is consistent with observations showing larger EMIC amplitudes near plasmaspheric plumes (de Soria-Santacruz et al. 2013; Chen et al. 2020). In plasmas containing heavy ions such as He^+ and O^+ , the EMIC wave spectrum exhibits stop bands at the gyrofrequencies of these species (Omidi et al. 2013; Chen et al.

2019), and the waves tend to become linearly polarized during propagation (Denton et al. 2014). Cold ions also influence ultra-low-frequency (ULF) waves by modifying plasma mass density and the corresponding Alfvén speed (Claudepierre et al. 2016).

EMIC waves are believed to play an important role in enhancing the flux of cold ions (Mauk 1982; Berchem & Gendrin 1985; Lu & Li 2007; Chen et al. 2018b; Li J et al. 2022; Li X et al. 2023; Liu et al. 2022; Kwon et al. 2023; Gamayunov et al. 2024; Kim et al. 2024). One mechanism is the nonresonant response, in which cold ions undergo $E \times B$ drift motion induced by wave electric fields (Gendrin & Roux, 1980; Liu et al. 2022; Kwon et al. 2023; Li et al. 2023; Kim et al. 2024). Numerical simulations have been conducted to investigate this process (Omidi et al. 2010; Kwon et al. 2023; Kim et al. 2024). Omidi et al. (2010) found that the enhancement occurs primarily perpendicular to the background magnetic fields. Kwon et al. (2023) suggested that EMIC waves can modulate the bulk flow of cold ions. Kim et al. (2024) further indicated that the enhancement is more significant for heavy ions than for protons. However, because these simulations were performed in uniform magnetic fields, the spatial evolution of cold-ion dynamics along field lines remains poorly understood. Another mechanism that has been proposed is resonant wave-particle interactions (Li et al. 2022, 2024; Zhang et al. 2025).

Using Magnetospheric Multiscale (MMS) data, Li et al. (2023) reported periodic enhancements in the energy flux and number density of cold protons, attributing these variations to a nonresonant response to EMIC waves. A corresponding proton phase-bunching distribution in the stationary gyrophase was also identified. In this study, we reanalyze this event with emphasis on the evolution of proton distributions. Nevertheless, satellite observations are also confined to fixed positions and cannot capture the spatial evolution of particle dynamics. In addition, the instruments have limited energy coverage, preventing them from fully resolving proton flux variations across all energies.

To address these observational limitations, we conduct a hybrid simulation in an inhomogeneous plasma system to model the spatial and temporal evolution of proton distributions in response to EMIC waves. Compared with previous studies assuming uniform magnetic fields, the present simulation provides a more realistic magnetic field topology for physical interpretation. The results reveal that flux enhancement is more significant at higher latitudes due to wave growth in amplitude. Despite this enhancement, the temperature and number density of cold protons remain nearly unchanged. Moreover, the proton phase-bunching distributions between nonresonant and resonant responses have been distinguished,

demonstrating that phase-bunching is a necessary but not sufficient condition for identifying resonant interactions with waves.

The organization of the paper is as follows. The observation dataset and analysis of the observational event are described in Sect. 2. The simulation model is described, and the simulation results are presented in Sect. 3. The proton dynamics in phase spaces are discussed in Sect. 4, and the major findings are summarized in Sect. 5.

2 MMS observations

2.1 Instrumentations

The MMS mission consists of four identical spacecraft in similar orbits, with perigees of $\sim 1.4 R_E$ and apogees between ~ 12 to $25 R_E$, where R_E denotes the Earth's radius. Each spacecraft is equipped with a Flux Gate Magnetometer (FGM; Russell et al. 2016) that measures triaxial magnetic fields in survey mode at 8 or 16 Hz. The Electric Field Double Probe (EDP; Ergun et al. 2016; Lindqvist et al. 2016) provides triaxial electric fields at 128 Hz and spacecraft potential at 32 Hz in fast survey mode. The Fast Plasma Investigation (FPI; Pollock et al. 2016) measures three-dimensional ion phase space distributions from ~ 10 eV to 30 keV in burst mode through its Dual Ion Spectrometer (DIS), with a time resolution of 150 ms and an angular resolution of 11.25° . The Hot Plasma Composition Analyzer (HPCA; Young et al. 2016) provides ion composition data. This study uses observations from MMS1.

2.2 Observational results

The cold-ion flux enhancement event reported by Li et al. (2023) was observed at L-shell ($L=9$), magnetic local time = 11.3, and magnetic latitude $\lambda=-1.6^\circ$, where the EMIC waves were identified as quasi-parallel and unidirectional. The background magnetic field B_0 is obtained using a low-pass filter with a cutoff frequency of 0.1 Hz. A cutoff of 0.05 Hz has also been tested and produces nearly identical results (not shown). Figure 1a shows the normalized disturbed magnetic fields $\delta B_{\perp 1}/B_{e0}$ and $\delta B_{\perp 2}/B_{e0}$, where $B_{e0}=73.2$ nT is the equatorial background magnetic field estimated from a dipole model. Figure 1b presents the omni-directional cold-ion energy flux. In the observations, the “ $\perp 1$ ” direction is defined as the cross product of B_0 and the sunward direction, and “ $\perp 2$ ” completes the orthogonal triad. As shown in Fig. 1a, EMIC waves exhibit a period of ~ 2.5 s and a normalized amplitude of $\sim 0.04 B_{e0}$. The minimum resonant energy for cyclotron resonance is ~ 1.5 keV (see Li et al. (2023)). Along with EMIC waves, the energy flux of ions with kinetic energy E_k ranging from several eV to several tens of eV, which is much lower than the minimum resonant energy, varies with the same period as the EMIC

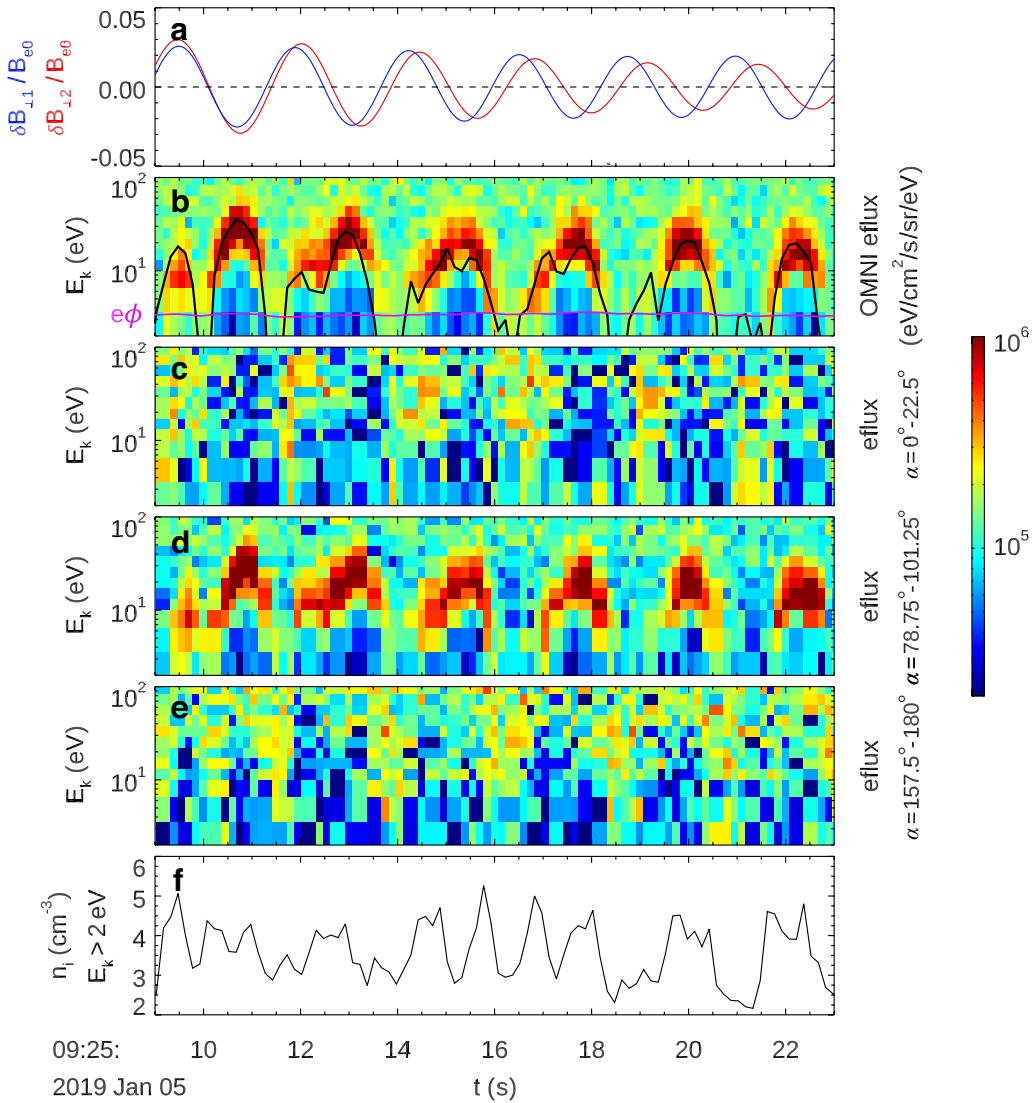


Fig. 1 MMS observations on 2019-01-05 from 09:25:09 to 09:25:23 UT. **(a)** Temporal evolution of $\delta B_{\perp 1}/B_{e0}$ (blue) and $\delta B_{\perp 2}/B_{e0}$ (red), with a black dashed line representing the zero value. **(b)** Omni-directional ion energy flux, with the energy $W_{E \times B}$ associate with $E \times B$ drift denoted by a black curve and the spacecraft potential ϕ indicated by a magenta curve. Ion energy fluxes in the pitch angle ranges: **(c)** $\alpha=0^\circ-22.5^\circ$, **(d)** $78.75^\circ-101.25^\circ$, and **(e)** $157.5^\circ-180^\circ$. **(f)** Time history of n_i for ions with $E_k > \sim 2$ eV

waves (Fig. 1b). The ion population is dominated by protons, since heavy ions contribute only $\sim 1\%$ of the proton density, according to the HPCA data. A series of energy-flux arcs coincides with the energy $W_{E \times B}$ (shown by the black curve in Fig. 1b) corresponding to $E \times B$ drift, defined as

$$W_{E \times B} = \frac{m_p v_d^2}{2} \quad (1)$$

where m_p is the proton mass, $v_d = \delta E \times B_0 / B_0^2$ is the drift speed, and δE is the wave electric field. Figures 1c–e illustrate the fluxes in the parallel, perpendicular, and

anti-parallel directions. The parallel and anti-parallel components exhibit similar variations and magnitudes. The perpendicular flux enhancement coincides with a marked decrease in the parallel and anti-parallel fluxes.

Figure 1f presents the ion number density n_i obtained from the DIS moments data of the FPI instrument and primarily contributed by protons. Note that due to the FPI detection threshold, only particles with $E_k > \sim 2$ eV are observed. For reference, the spacecraft potential ϕ is ~ 3.5 V (magenta curve in Fig. 1b) during the interval, as measured by the EDP instrument, which is consistent with the lower energy limit. The density exhibits periodic

variations from ~ 2 to $\sim 5 \text{ cm}^{-3}$ and these variations coincide with the enhancements in energy flux. An exception appears between 14 and 18 s, during which n_i might be affected by other waves. The oscillation frequency of n_i is $\sim 0.39 \text{ Hz}$, corresponding to a period of $\sim 2.5 \text{ s}$, matching that of EMIC waves. This will be further discussed in Sect. 3.2 using simulation data.

Figure 2a shows the temporal evolution of drift velocity v_{d1} in the “ $\perp 1$ ” direction, which oscillates periodically between positive and negative values. Five time points within a single period are selected: $t1=14.42 \text{ s}$, $t2=15.17 \text{ s}$, $t3=15.77 \text{ s}$, $t4=16.07 \text{ s}$, and $t5=16.67 \text{ s}$, with the corresponding v_{d1} values marked by magenta crosses. Figure 2b illustrates the proton phase space density $f(v_{||}, v_{\perp 1})$ at these time points, showing the slice at $v_{\perp 2}=0$, where only particles with $E_k > 2 \text{ eV}$ (velocity $> 19.6 \text{ km/s}$) are measured. The peak of f is near $v_{||}=0$, while in $v_{\perp 1}$ it oscillates between positive and negative values, consistent with the v_{d1} evolution, indicating that the bulk flow of cold protons responds to the $E \times B$ drift induced by EMIC waves.

We further conduct a simulation in a dipole field to investigate the cold-proton flux fluctuations and the corresponding spatial and temporal evolution of particle dynamics. Note that the simulation aims to examine the general physics of particle response to EMIC waves in the Earth’s magnetosphere, rather than focusing solely

on quantitatively accounting for a specific observational event.

3 Hybrid simulation in a dipole field

3.1 Simulation model

We perform a one-dimensional (1-D) hybrid simulation using the general curvilinear plasma simulation code (GCPIC) model (Kang et al. 2021; Wang et al. 2024; Chen et al. 2025) in a dipole field to simplify the inhomogeneous magnetospheric plasma system (Lee & Hudson 2001; Meredith et al. 2012). The simulation domain follows a magnetic field line at $L=6$, covering a magnetic latitude range of $\lambda \sim -30^\circ$ to $\sim 30^\circ$. Ions are treated kinetically as particles, while electrons are modeled as a resistive, massless fluid, with charge neutrality maintained. Reflecting boundary conditions are applied to both fields and particles.

Typical magnetospheric plasma parameters are adopted. At the magnetic equator, the background magnetic field is $B_{e0}=144 \text{ nT}$ and the plasma density is $n_{e0}=20 \text{ cm}^{-3}$ (Carpenter & Anderson 1992; Denton et al. 2004), yielding an equatorial Alfvén speed $V_{A0}=B_{e0}/\sqrt{\mu_0 n_{e0} m_p}=702 \text{ km/s}$ and a ratio of the plasma frequency to the equatorial electron gyrofrequency, $\omega_{pe}/\Omega_{e0}=9.97$, where $\omega_{pe}=\sqrt{n_{e0} e^2/(m_e \epsilon_0)}$ and $\Omega_{e0}=B_{e0} e/m_e$, with μ_0 and ϵ_0 the vacuum permeability and permittivity, m_e the electron mass, and e the elementary charge. The plasma contains both hot and

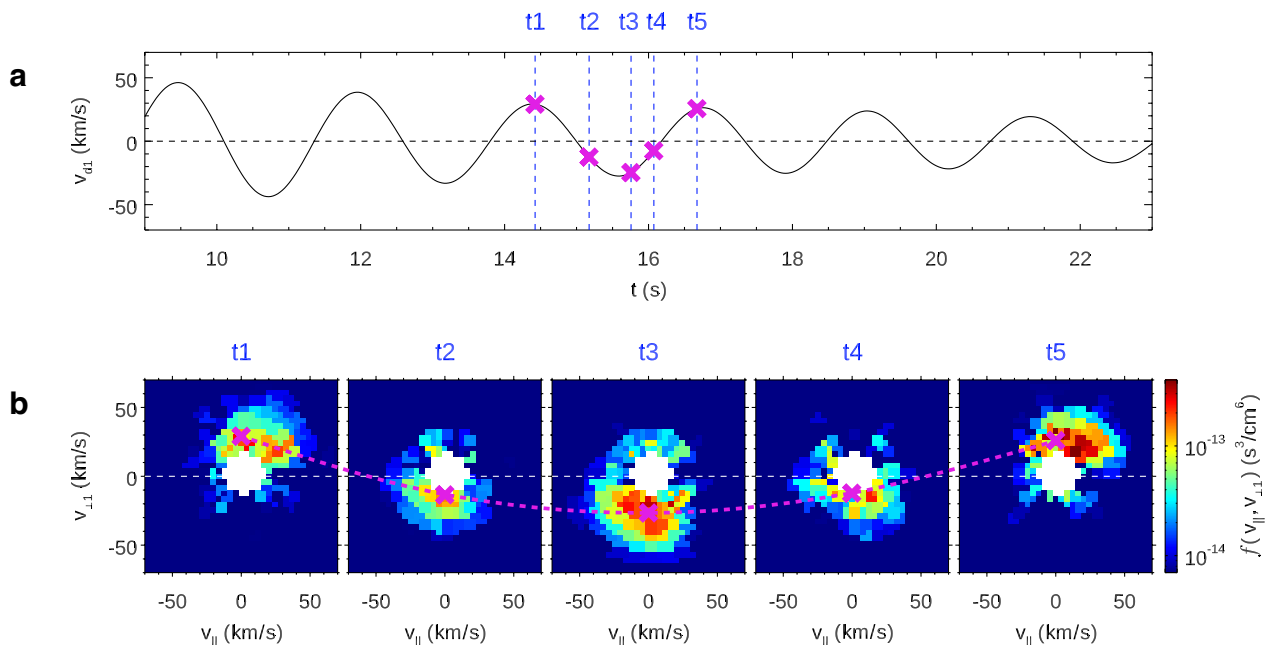


Fig. 2 MMS observations of ion phase space density. **a** Temporal evolution of v_{d1} , with selected time points ($t1-t5$) indicated by blue dashed lines and corresponding v_{d1} values marked by magenta crosses. **b** Phase space density $f(v_{||}, v_{\perp 1})$ at the selected times for the slice $v_{\perp 2}=0$. The magenta crosses indicate $(0, v_{d1})$, which are smoothly connected by a magenta dashed curve. The black/white dashed lines in all panels represent zero

cold protons. Hot protons follow a subtracted Maxwellian distribution, with the equatorial distribution function given by

$$f(u_{||}, u_{\perp}) = \frac{n_{heq}}{(2\pi)^{3/2} U_{t||} U_{t\perp}^2 (1 - \rho\beta)} \exp\left(-\frac{u_{||}^2}{2U_{t||}^2}\right) \cdot \left[\exp\left(-\frac{u_{\perp}^2}{2U_{t\perp}^2}\right) - \rho \exp\left(-\frac{u_{\perp}^2}{2\beta U_{t\perp}^2}\right) \right] \quad (2)$$

where $\rho=1$ and $\beta=0.3$, $u_{||}=\gamma v_{||}$ and $u_{\perp}=\gamma v_{\perp}$ are the parallel and perpendicular momentum, $U_{t||}$ and $U_{t\perp}$ are the parallel and perpendicular thermal momentum, γ is the relativistic factor, and n_{heq} is the equatorial number density. At the magnetic equator, hot protons exhibit $n_{heq}/n_{e0}=0.05$, parallel temperature $T_{||}=m_p U_{t||}^2=20$ keV (Kim et al. 2024), and temperature anisotropy $T_{\perp}/T_{||}=U_{t\perp}^2/U_{t||}^2=2.0$ (Yue et al. 2019). Parameters along the field line follow Liouville's theorem (Summers et al. 2012). Cold protons are isotropic with a temperature of 10 eV (Kim et al. 2024).

The simulation domain comprises 4000 grid cells with a grid length of $\Delta q=0.12$ $V_{A0}/\Omega_{p0}=6.11$ km ($\Omega_{p0}=eB_{e0}/m_p$ is the equatorial proton gyrofrequency). Each grid contains 4000 particles. The time step is $\Delta t=2.7 \times 10^{-3} \Omega_{p0}^{-1}$, corresponding to a realistic value of 2.0×10^{-4} s.

3.2 Simulation results

Figure 3a illustrates the disturbed magnetic field $\delta B^2/B_{e0}^2$ in the $\lambda-t$ plane, with $\delta B^2=\delta B_{\perp 1}^2+\delta B_{\perp 2}^2$. The magnetic

latitude $\lambda=11.4^\circ$ is highlighted by a black vertical dashed line. In the simulation, “ $\perp 1$ ” and “ $\perp 2$ ” denote the radial and azimuthal directions, respectively. EMIC waves are excited near the magnetic equator at $t\sim 7$ s and propagate towards higher latitudes, growing in amplitude. They reflect at boundaries at ~ 30 s; to avoid interference, only particle dynamics before the reflection are analyzed. Figure 3b shows the temporal evolution of $\delta B_{\perp 1}/B_{e0}$ and $\delta B_{\perp 2}/B_{e0}$ at $\lambda=11.4^\circ$, where a high-frequency oscillation is modulated by a low-frequency signal. The high-frequency oscillation, identified as EMIC waves (or Pc1 ULF waves; Jacobs et al. 1964), has a period of $\sim 1-2$ s. While the low-frequency oscillation, identified as Pc3 ULF waves, has a longer period of ~ 20 s. The presence of both wave types is evident in the $\omega-t$ spectrum (Fig. 3c), calculated using the fast Fourier transform (FFT) with an FFT window of ~ 8 s. EMIC waves appear at $t\sim 10$ s and exhibit a rising-tone chirping, with frequency increasing from $\sim 0.20 \Omega_{p0}$ to $\sim 0.45 \Omega_{p0}$ between $t\sim 14$ to ~ 25 s. Using the cyclotron resonance condition, the minimum

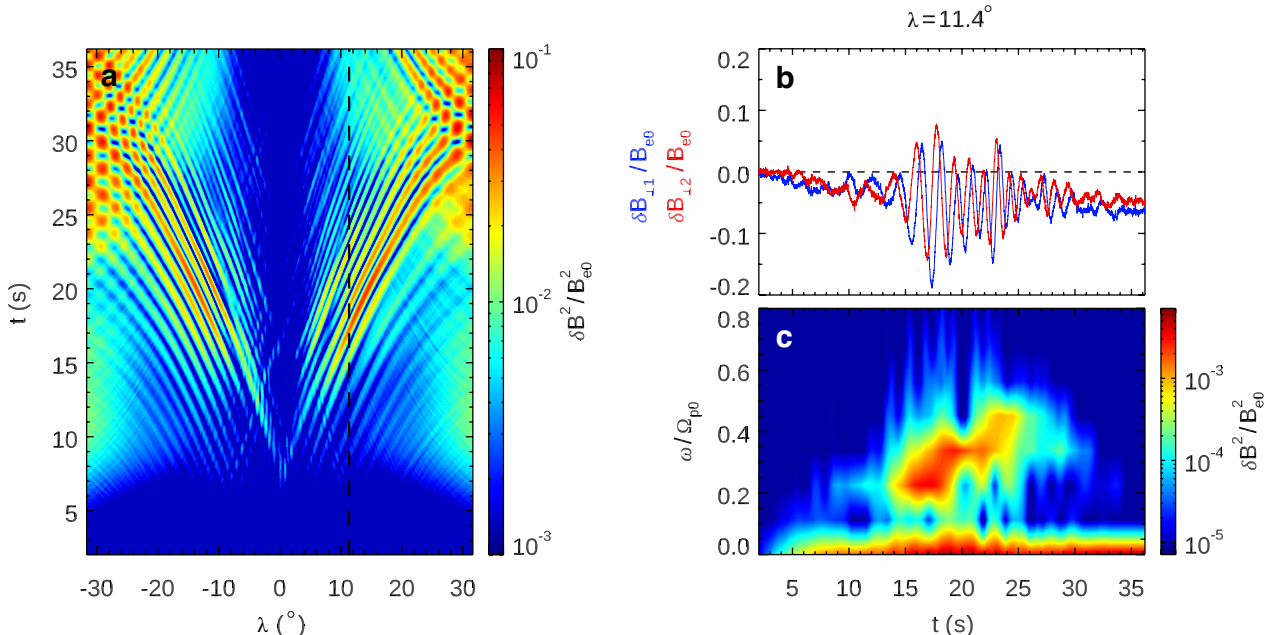


Fig. 3 Simulation results of the wave spectrum. **a** Disturbed magnetic field $\delta B^2/B_{e0}^2$ in the $\lambda-t$ plane. The black vertical dashed line marks $\lambda=11.4^\circ$. **b** Temporal evolutions of $\delta B_{\perp 1}/B_{e0}$ (blue) and $\delta B_{\perp 2}/B_{e0}$ (red) at $\lambda=11.4^\circ$. The black horizontal dashed line denotes zero. **c** Corresponding $\omega-t$ spectrum of $\delta B^2/B_{e0}^2$.

resonant energy is estimated as ~ 10 keV (~ 2 keV) for the waves with frequencies of $0.20 \Omega_{p0}$ ($0.45 \Omega_{p0}$). The Pc3 ULF waves, with a frequency of $\sim 0.02 \Omega_{p0}$ (estimated using a longer FFW window of ~ 32 s), appear earlier at $t \sim 4$ s and persist continuously. This study focuses on EMIC waves, while the excitation and effects of Pc3 ULF waves are reserved for future work.

We first analyze the particle dynamics at $\lambda = 11.4^\circ$. Figures 4b–e show cold-proton energy fluxes in the omni, parallel, perpendicular, and anti-parallel directions, respectively, with $\delta B_{\perp 1}/B_{e0}$ and $\delta B_{\perp 2}/B_{e0}$ plotted in Fig. 4a for reference. As shown in Fig. 4b, the energy flux of protons with E_k from a few eV to ~ 200 eV varies

significantly, displaying periodic arcs consistent with observations (Fig. 1b). These protons cannot resonate with EMIC waves due to their low E_k . The flux modulation timescale is firstly ~ 2 s and later decreases to ~ 1 s, matching the rising-tone chirping of EMIC waves. The simulated energy $W_{E \times B}$ (black curve in Fig. 4b) agrees well with the flux modulation, which occurs primarily in the perpendicular direction (Fig. 4d). Therefore, the observed periodic flux variation of cold protons is reproduced in the simulation.

Figure 5a depicts the periodic oscillation of drift velocity v_{d1} of cold protons. Five time points within one period are selected: $T1 = 20.05$ s, $T2 = 20.45$ s, $T3 = 20.74$ s,

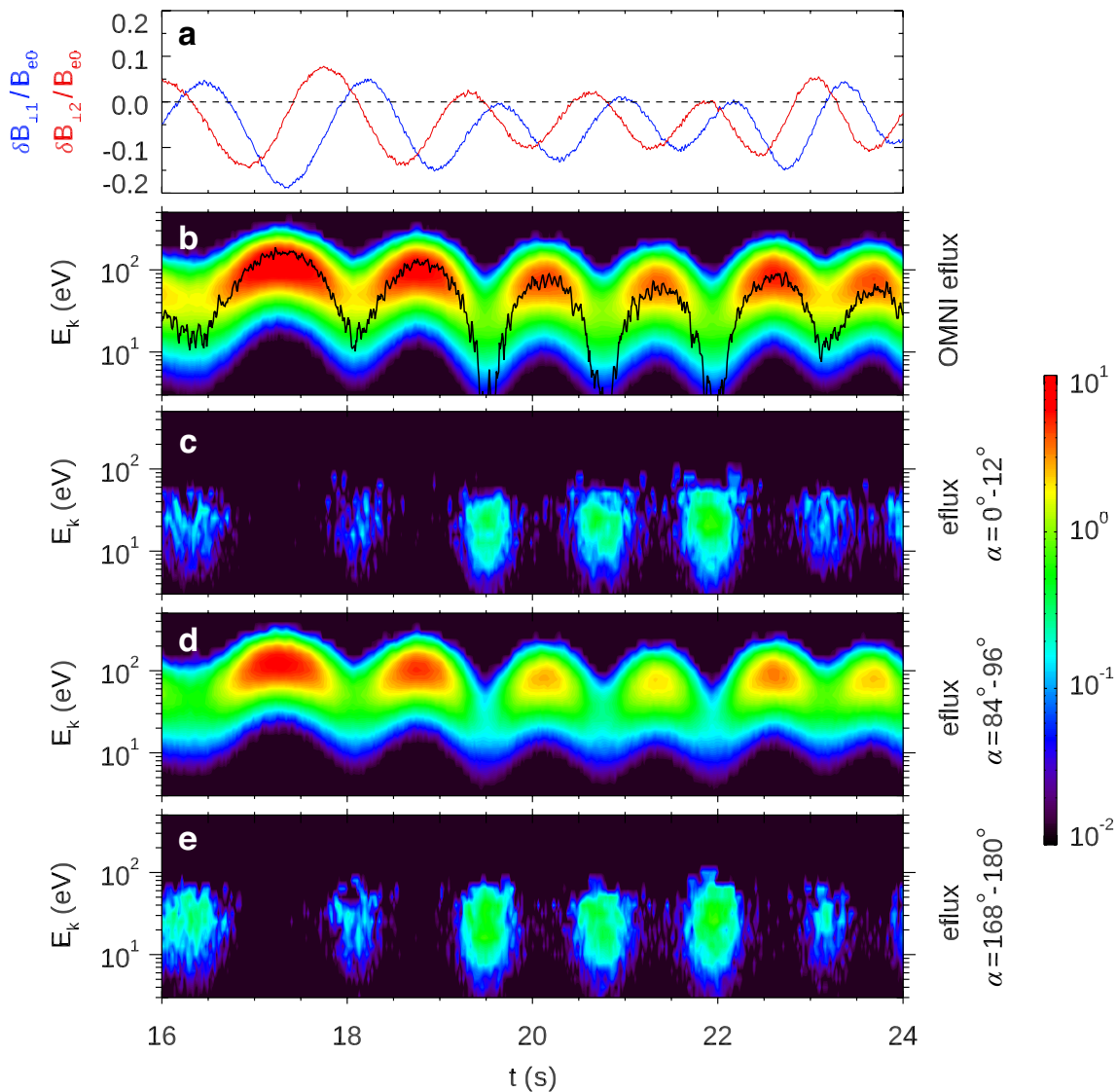


Fig. 4 Simulation results of cold-proton energy fluxes at $\lambda = 11.4^\circ$. **a** Temporal evolutions of $\delta B_{\perp 1}/B_{e0}$ (blue) and $\delta B_{\perp 2}/B_{e0}$ (red); the black dashed line denotes zero. **b** Omni-directional cold-proton energy flux with $W_{E \times B}$. Energy fluxes in the pitch angle ranges: **(c)** $\alpha = 0^\circ - 12^\circ$, **(d)** $84^\circ - 96^\circ$, and **(e)** $168^\circ - 180^\circ$

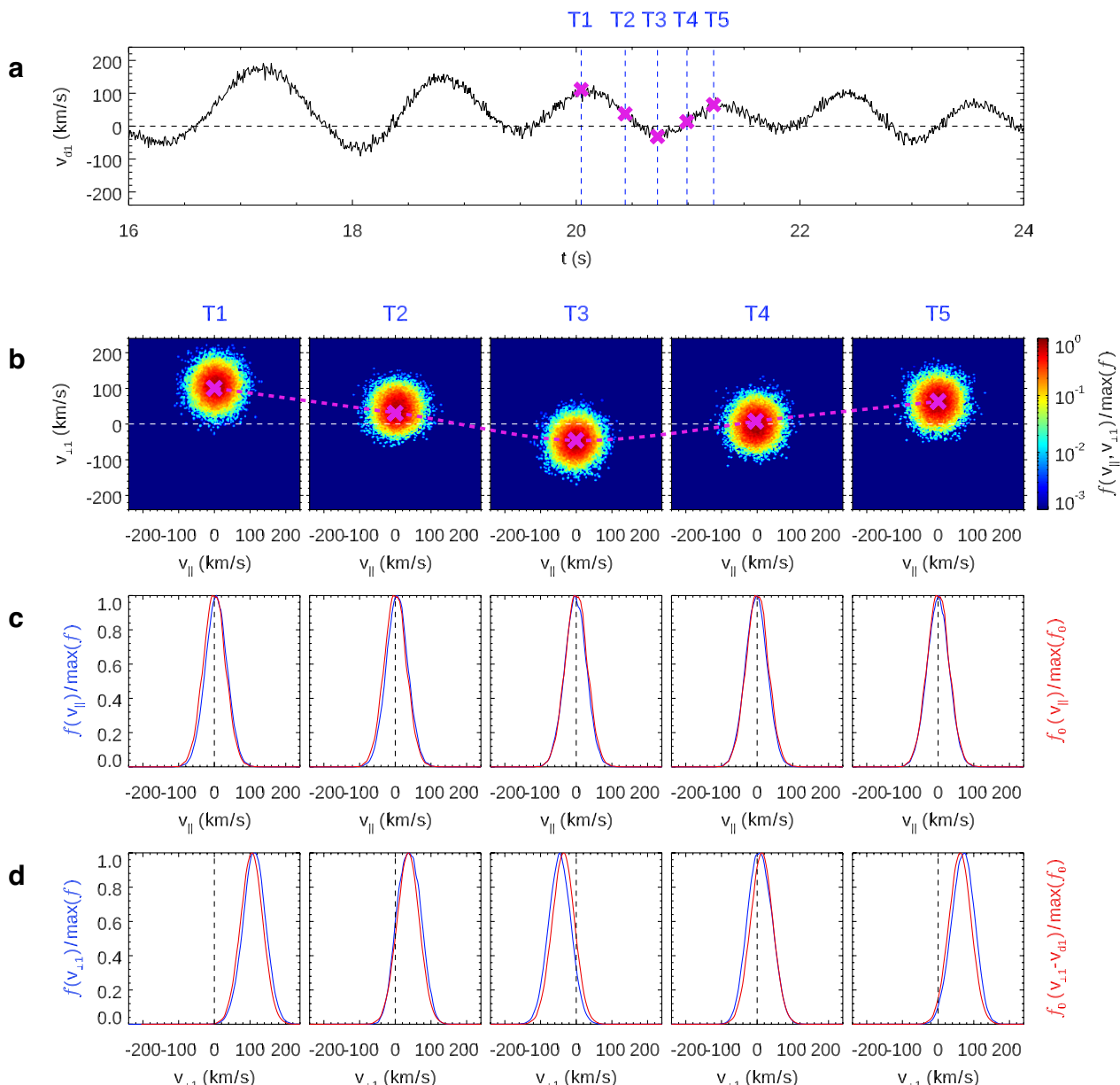


Fig. 5 Simulated phase space density of cold protons at $\lambda=11.4^\circ$. (a) Temporal evolution of v_{d1} , with selected time points (T1-T5) indicated by blue dashed lines and corresponding v_{d1} values marked by magenta crosses. Normalized (b) phase space density $f(v_{||}, v_{\perp 1})$ for the slice $v_{\perp 2}=0$, (c) parallel phase space density $f(v_{||})$ in blue, and (d) perpendicular phase space density $f(v_{\perp 1})$ in blue, at the selected times. In each panel, the dashed white/black lines denote zero. In panel (b), the magenta crosses indicate $(0, v_{d1})$, connected by a magenta dashed curve. In panel (c), the red curves show the initial parallel velocity distribution $f_0(v_{||})$. In panel (d), the red curves represent the initial perpendicular velocity distribution shifted by the drift velocity $f_0(v_{\perp 1} - v_{d1})$.

T4=20.90 s, and T5=21.23 s. The cold-proton phase space density $f(v_{||}, v_{\perp 1})$ at these times is shown in Fig. 5b for the slice $v_{\perp 2}=0$. In the parallel direction, f is centered around $v_{||}=0$. However, in the $v_{\perp 1}$ direction, its center shifts from positive to negative and back to positive, consistent with the variation of v_{d1} .

The phase space densities $f(v_{||})$ and $f(v_{\perp 1})$ are shown in Figs. 5c, d, respectively. In the parallel direction, $f(v_{||})$ closely resembles the initial distribution $f_0(v_{||})$. In the perpendicular direction, $f(v_{\perp 1})$ maintains a Gaussian shape but exhibits a nonzero bulk flow that oscillates with time. For comparison, the initial distribution $f_0(v_{\perp 1})$ is shifted according to the magnitude and sign of v_{d1} . The

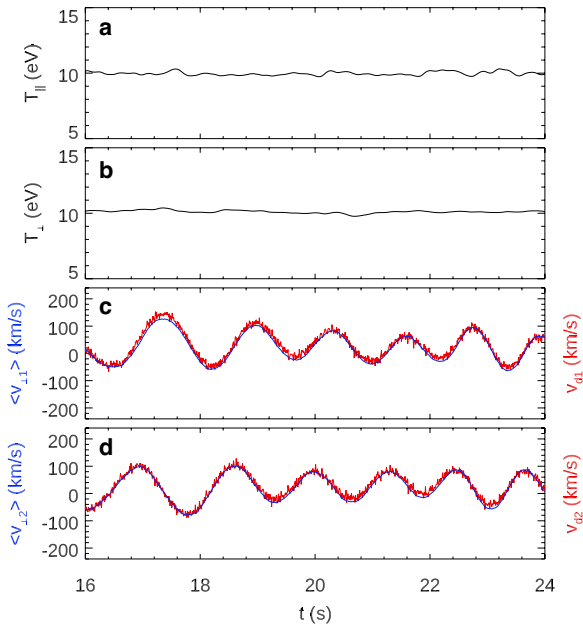


Fig. 6 Simulated temporal evolutions of (a) $T_{||}$ and (b) T_{\perp} for cold protons. The perpendicular bulk flow velocities (c) $\langle v_{\perp 1} \rangle$ and (d) $\langle v_{\perp 2} \rangle$, colored in blue, with the red curves representing the drift velocities v_{d1} and v_{d2}

strong overlap between $f(v_{\perp 1})$ and $f_0(v_{\perp 1} - v_{d1})$ indicates that the evolution of perpendicular velocity distribution is determined by $E \times B$ drift motion.

Further quantitative evidence is given in Fig. 6, which shows the temporal evolutions of parallel temperature $T_{||}$ (Fig. 6a) and perpendicular temperature T_{\perp} (Fig. 6b) for cold protons. In the simulation, $T_{||}$ and T_{\perp} are calculated as

$$T_{||} = \frac{m_p}{2} \langle (v_{||} - \langle v_{||} \rangle)^2 \rangle \quad (3)$$

$$T_{\perp} = \frac{m_p}{4} \left[\langle (v_{\perp 1} - \langle v_{\perp 1} \rangle)^2 \rangle + \langle (v_{\perp 2} - \langle v_{\perp 2} \rangle)^2 \rangle \right] \quad (4)$$

where $\langle v_{||} \rangle$ is the bulk flow velocity in the parallel direction, $\langle v_{\perp 1} \rangle$ and $\langle v_{\perp 2} \rangle$ are the bulk flow velocities in perpendicular directions, and $\langle \dots \rangle$ denotes the average over all cold protons in a grid. Both $T_{||}$ and T_{\perp} remain nearly unchanged during flux enhancement and are close to the initial value of 10 eV. The temporal profiles of $\langle v_{\perp 1} \rangle$ and $\langle v_{\perp 2} \rangle$ are shown in blue in Figs. 6c and d, respectively, with v_{d1} and v_{d2} overplotted in red. The close agreement between $\langle v_{\perp 1} \rangle$ and v_{d1} (and between $\langle v_{\perp 2} \rangle$ and v_{d2}) demonstrates that the bulk flow of cold protons oscillates in response to EMIC waves.

We also investigate the cold proton dynamics at different magnetic latitudes. Figures 7a–d illustrate the

omni-directional proton energy fluxes at $\lambda=17.8^\circ$, 14.6° , 7.1° , and 4.0° , respectively, with $W_{E \times B}$ overplotted. The flux variations at all latitudes track the evolution of $W_{E \times B}$ evolution. At lower latitudes, flux increases at energies of a few tens of eV, while at higher latitudes the enhancement extends to ~ 200 eV. Moreover, the enhancement is more significant at higher latitudes. These differences are primarily due to wave amplitude (δE or δB), which grows during propagation and saturates near $\lambda \sim 10^\circ$ (Fig. 3a). Specifically, $\delta B/B_{e0}$ is ~ 0.05 at $\lambda=4^\circ$ and increases 4 times to ~ 0.2 at $\lambda=10^\circ$. Although B_0 also increases with latitude, this rise is moderate (~ 1.7 times from $\lambda=0^\circ$ to $\lambda=20^\circ$), resulting in minimal impact on $W_{E \times B}$.

In observations, the cold proton number density n_i exhibits temporal oscillations (Fig. 1f). We further examine the simulated n_i , where an E_k threshold is applied to collect particles. Figure 8a shows the omni-directional energy flux at $\lambda=11.4^\circ$, with a magenta dashed line indicating the 10 eV threshold. Figure 8b presents the temporal evolution of n_i for cold protons with $E_k > 10$ eV and for all cold protons. The n_i with $E_k > 10$ eV exhibits periodic variations from $\sim 10 \text{ cm}^{-3}$ to $\sim 19 \text{ cm}^{-3}$, coinciding with the flux enhancement, whereas the total number density remains nearly constant at $\sim 19 \text{ cm}^{-3}$ ($0.95 n_{e0}$). This discrepancy arises from the satellite detection threshold, which excludes lower-energy particles. When $E \times B$ drift is negligible, particles with E_k below the threshold are not included in the density calculation. However, when the drift becomes significant, all particles experience a large bulk flow, causing those previously below the threshold to shift above it, thereby reducing the difference between the two densities. This quantification indicates that the observed density oscillation is due to instrumental limitations rather than any physical mechanism.

Nevertheless, the total number density shows spatial fluctuations. Figures 8c and d show the wave field $\delta B_{\perp 1}/B_{e0}$ and total cold proton density n_i as a function of h at $t=12.1$ s, where h represents the distance along the field line to the magnetic equator. The n_i fluctuates around the magnetic equator with a spatial scale of $\sim 5 V_{A0}/\Omega_{p0}$, about half of the EMIC wavelength ($\sim 10 V_{A0}/\Omega_{p0}$). This fluctuation results from nonlinear wave-wave coupling, where counter-propagating waves generate an electrostatic standing structure with zero frequency and double wave number (Chen et al. 2018a; Gao et al. 2018). The zero-frequency, double-wave number signatures are also present in $\delta E_{||}$ and $v_{||}$ data (not shown).

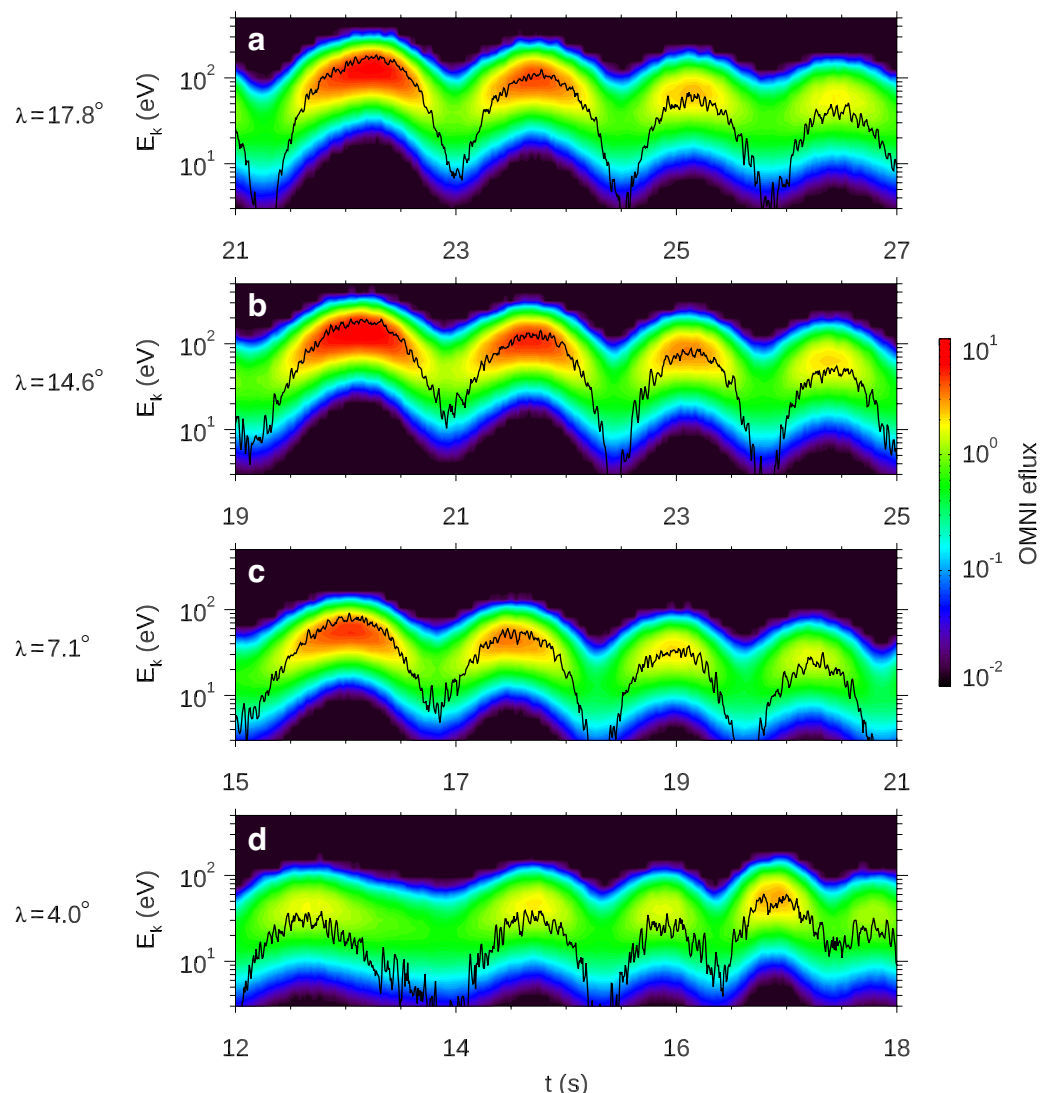


Fig. 7 Simulated omni-directional cold-proton energy fluxes from higher latitudes (top) to lower latitudes (bottom). In each panel, the black curve indicates the corresponding $W_{E \times B}$

4 Discussions

Recent studies have reported phase-bunching distribution of cold protons in the stationary gyrophase, characterized by inclined stripe patterns (Liu et al. 2022; Li J et al. 2022, 2024; Li X et al. 2023). To examine this phenomenon, we analyze proton dynamics in the stationary gyrophase using the simulation data. Figure 9a shows the phase space density $f(t, \varphi_{v\perp})$ of cold protons at $\lambda = 11.4^\circ$, with green and orange dots marking the phase angles $\varphi_{-\delta B}$ and $\varphi_{-\delta E}$, respectively. Here, $\varphi_{v\perp}$ represents the phase angle of $v\perp$ in the stationary gyrophase, while $\varphi_{-\delta B}$ and $\varphi_{-\delta E}$ are the phase angles of $-\delta B$ and $-\delta E$, respectively. The cold protons exhibit a nonresonant response to waves and they are phase-bunched following $\varphi_{-\delta B}$, indicating the

phase difference between $v\perp$ and δB of $\zeta=\pi$. A theoretical explanation for the phase-bunching at $\zeta=\pi$ is provided in Appendix A.

Li et al. (2024) suggested that the phase-bunched behavior of cold protons at $\varphi_{-\delta B}$ (or $\zeta=\pi$) results from resonant interaction with waves when the wave amplitude is comparable with the background magnetic field. Their observations were made near the bow shock, where the plasma exhibits a bulk flow velocity much higher than that in the magnetosphere, the region in which our simulation is performed. Although the phase-bunching pattern in our simulation resembles theirs, the cold protons are demonstrated to be fully nonresonant and such a phase-bunching is just a linear response to waves.

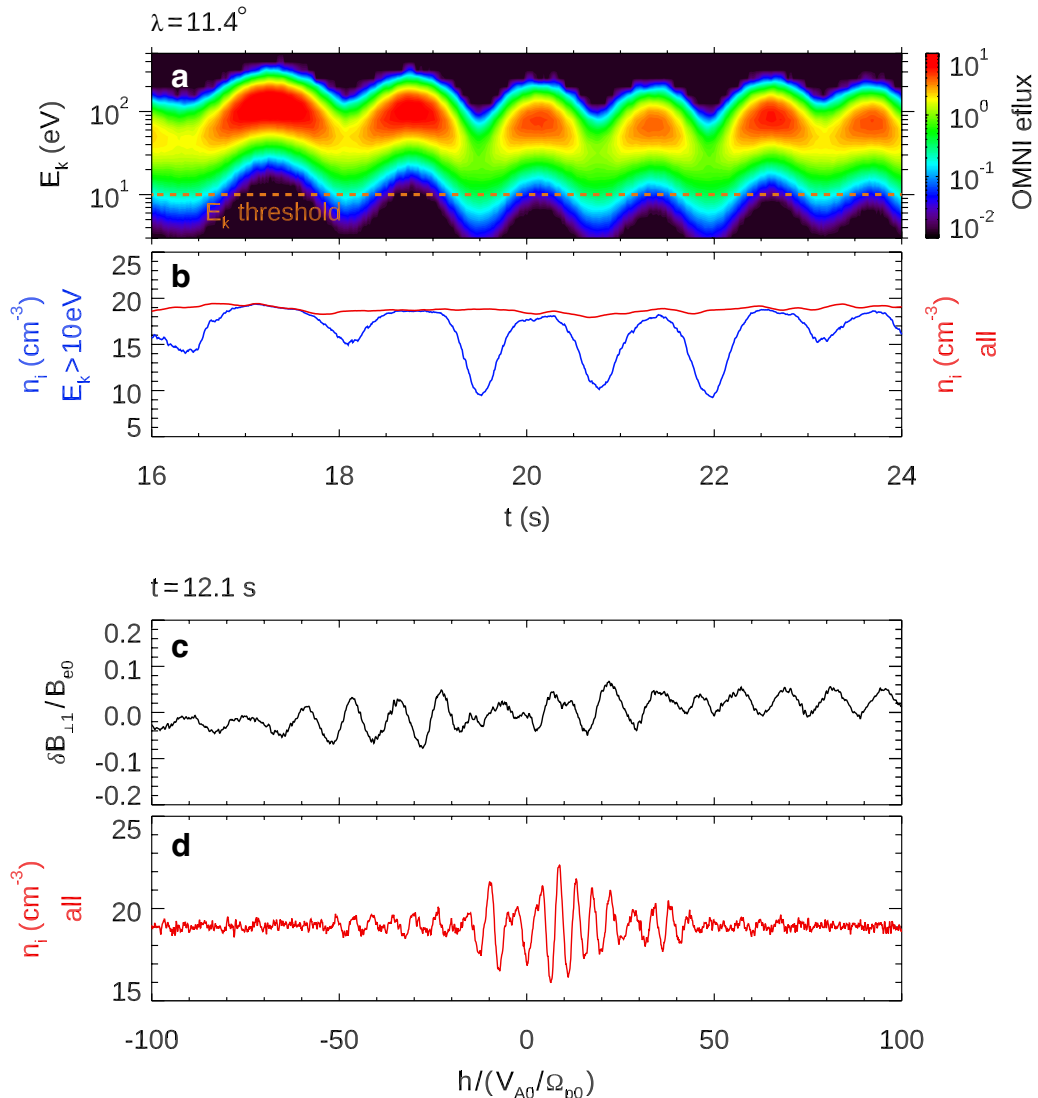


Fig. 8 Cold proton number density in simulation. (a) Omni-directional energy flux, with E_k threshold denoted by the orange dashed line. (b) Temporal evolution of n_i for cold protons with $E_k > 10 \text{ eV}$ (blue) and for all cold protons (red) at $\lambda = 11.4^\circ$. (c) Wave field $\delta B_{\perp 1}/B_{e0}$ and (d) total cold proton density n_i as a function of h at $t = 12.1 \text{ s}$. For reference, $h/(V_{A0}/\Omega_{p0}) = 50$ corresponds to a magnetic latitude of $\lambda = 7.6^\circ$.

The modified cyclotron resonance condition, which accounts for the influence of wave amplitude, is given by (Chen & Bortnik 2020; Li et al. 2022)

$$\omega - kv_c - \Omega_p + \frac{\Omega_1 \cos \zeta}{v_{\perp}} \left(v_c - \frac{\omega}{k} \right) = 0 \quad (5)$$

where $\Omega_1 = e\delta B/m_p$, $\Omega_p = B_0 e/m_p$ is the local gyrofrequency, and v_c is the cyclotron resonant velocity. Using parameters $\omega/\Omega_{p0} = 0.25$, $kV_{A0}/\Omega_{p0} = 0.64$, $\zeta = \pi$, $v_{\perp}/V_{A0} = 2.5$, and $\delta B/B_{e0} = 0.2$, the estimated v_c at $\lambda = 15^\circ$ is $-1.48 V_{A0}$ ($= -1039 \text{ km/s}$). We collect particles at $\lambda = 11.4^\circ$ and

record their information from $t = 19.7 \text{ s}$. Figures 9b-d present the trajectories of a cold proton in the $\zeta - v_{||}$, $v_{\delta B} - v_{\delta E}$, and $-v_{\delta B} - v_d - v_{\delta E}$ planes, where $v_{\delta B}$ and $v_{\delta E}$ are the perpendicular velocities along δB and δE . In Fig. 9b, the proton has a parallel velocity of $v_{||} \sim 30 \text{ km/s}$, much smaller than $|v_c|$. In the $v_{\delta B} - v_{\delta E}$ plane (Fig. 9c), the particle rotates clockwise around the guiding center, with a large $v_{\delta B}$ in the $-\delta B$ direction due to $E \times B$ drift. Consequently, its phase angle ζ remains confined near π . However, because of the small $v_{||}$, the proton cannot maintain phase synchrony with the waves. The gyromotion period ($\sim 0.5 \text{ s}$) is shorter than the EMIC wave period ($> 1 \text{ s}$), so the proton experiences continuously varying wave

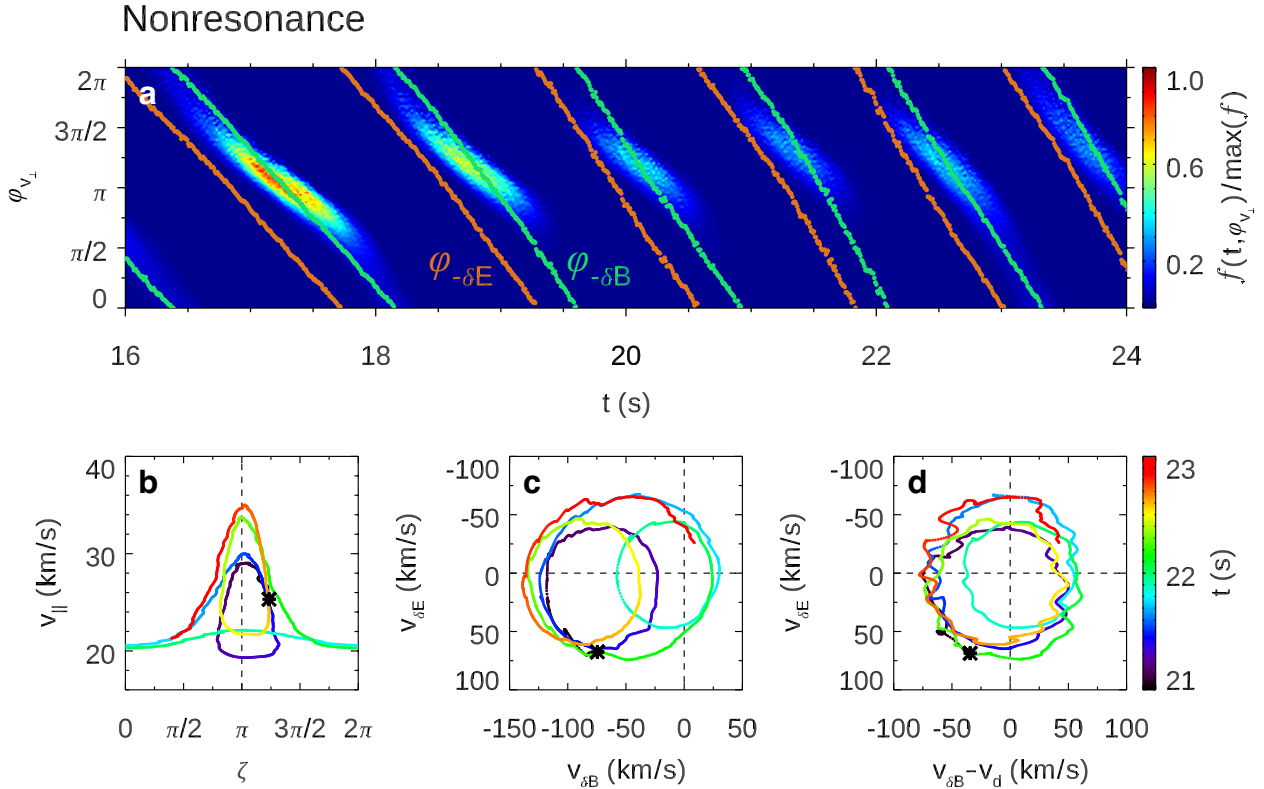


Fig. 9 Simulated gyrophase signals of cold protons. (a) Normalized phase space density $f(t, \varphi_{v_\perp})$ for cold protons at $\lambda = 11.4^\circ$. The orange and green dots denote $\varphi_{-\delta E}$ and $\varphi_{-\delta B}$, respectively. Trajectories of a cold proton in the (b) ζ - v_\parallel , (c) $v_{\delta B}$ - $v_{\delta E}$, and (d) $v_{\delta B} - v_d$ - $v_{\delta E}$ planes, with asterisks marking the starting point. In panels (b-d), different colors represent temporal evolution. In panel (b), the black vertical dashed line denotes $\zeta=\pi$. In panels (c-d), the black vertical/horizontal dashed line indicates zero

phases. After removing the drift velocity v_d (Fig. 9d), the trajectory centers around $(0, 0)$, with nearly constant v_\perp and a clockwise rotation of ζ from 2π to 0 . Therefore, the phase-bunching distribution of cold protons in stationary gyrophase arises from the drift motion in $-\delta\mathbf{B}$ direction. Once this drift is removed, the phase-bunching disappears, indicating the lack of resonant interaction between cold protons and EMIC waves.

For comparison, the phase-bunching of hot protons is illustrated in Fig. 10a. These protons undergo cyclotron resonance with EMIC waves and are phase-bunched following $\varphi_{-\delta E}$. Figures 10b-d show the trajectory of a hot proton, where the paths in Fig. 10c and d appear nearly identical because $v_d \ll v_\perp$. Without resonance, the particle's v_\perp rotates clockwise, leading to a monotonic decrease of ζ from 2π to 0 . During $t=20.6-21.1$ s, when $v_\parallel \sim v_c$, however, v_\perp starts to rotate counterclockwise from $\zeta \sim 3\pi/2$ and then returns to clockwise rotation, forming a crescent-shaped trajectory (highlighted by the arrows in Fig. 10c and d). This behavior results from nonlinear wave-particle interactions through cyclotron resonance (Chen et al. 2024), during which the particle's $|v_\parallel|$ decreases (indicated by the arrow in Fig. 10b) and E_k (or v_\perp) increases due to

the positive δE around $\zeta=3\pi/2$. In contrast, hot protons around $\zeta=\pi/2$ experience a reduction in E_k because of the negative δE (not shown). Therefore, hot protons can be trapped in wave phases and exchange energy with waves through cyclotron resonance. Similar nonlinear wave-particle interactions involving cyclotron resonance with hot ions have been reported in observations (Shoji et al. 2017; Kitamura et al. 2018; Asamura et al. 2021).

The phase-bunched behavior of cold and hot protons at different ζ affects their energy transfer with waves. The phase space density of cold protons in the ζ - v_\parallel plane at $t = 18.7$ s is shown in Fig. 11a, with particles centered at $\zeta=\pi$ and $v_\parallel=0$. Figure 11b illustrates the differential resonant current J_E^D of cold protons, calculated as (Chen et al. 2023)

$$J_E^D = \int_0^\infty e v_\perp \cdot \delta \hat{\mathbf{E}} f(u_\parallel, \zeta, u_\perp) u_\perp du_\perp \quad (6)$$

where $\delta \hat{\mathbf{E}}$ is the unit vector of δE and $f(u_\parallel, \zeta, u_\perp)$ represents the phase space density. Note that J_E^D is the differential form of resonant current along electric field J_E (Omura 2021), with positive (negative) values indicating particle energy gain from waves (energy transfer to

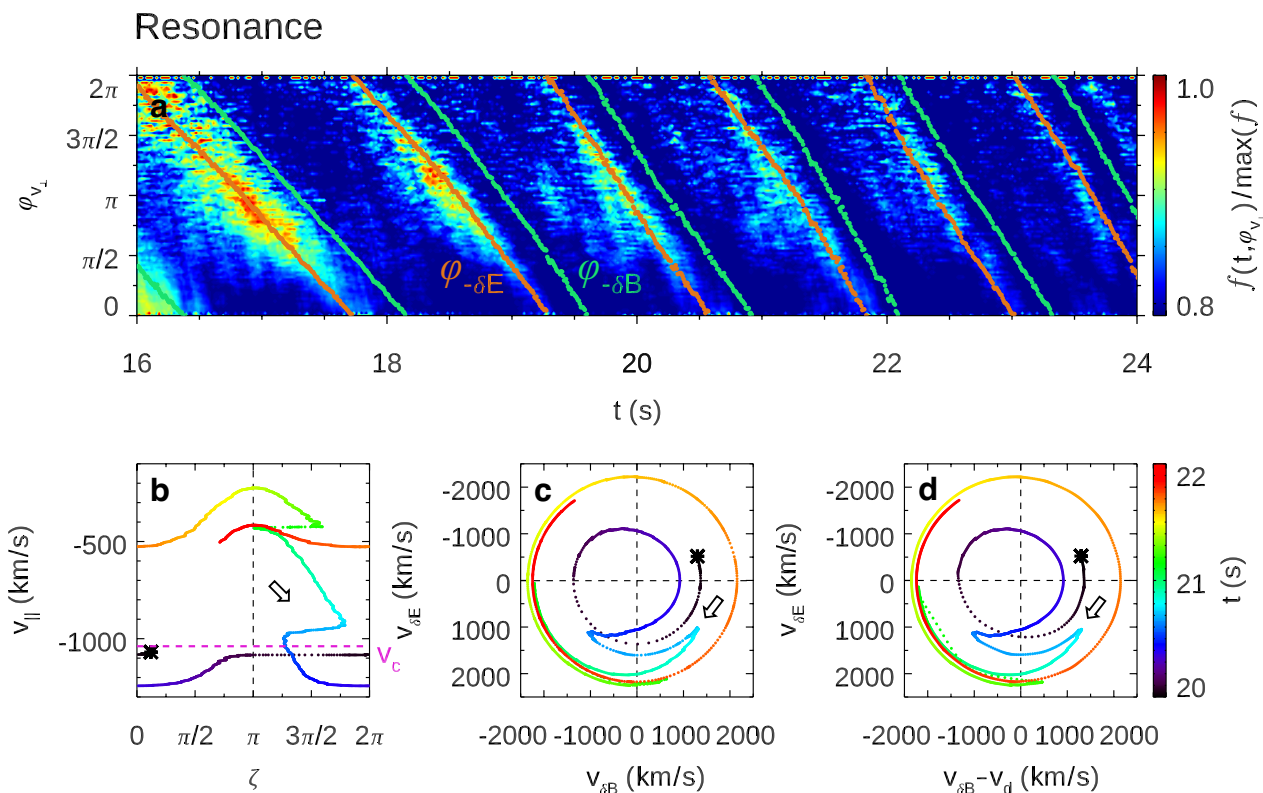


Fig. 10 Simulated gyrophase signals of hot protons. **a** The normalized $f(t, \varphi_{v_\perp})$ at for hot protons $\lambda = 11.4^\circ$. Trajectories of a hot proton in the **(b)** ζ - v_\parallel , **(c)** $v_{\delta B}$ - $v_{\delta E}$, and **(d)** $v_{\delta B} - v_d$ - $v_{\delta E}$ planes, respectively, with asterisks marking the starting point. In panel **(b)**, the magenta horizontal dashed line marks v_c and the black vertical dashed line denote $\zeta=\pi$. In panels **(c-d)**, the black horizontal/vertical dashed line indicates zero. The arrows in panels **(b-d)** highlight the interval $t=20.6-21.1$ s of cyclotron resonance

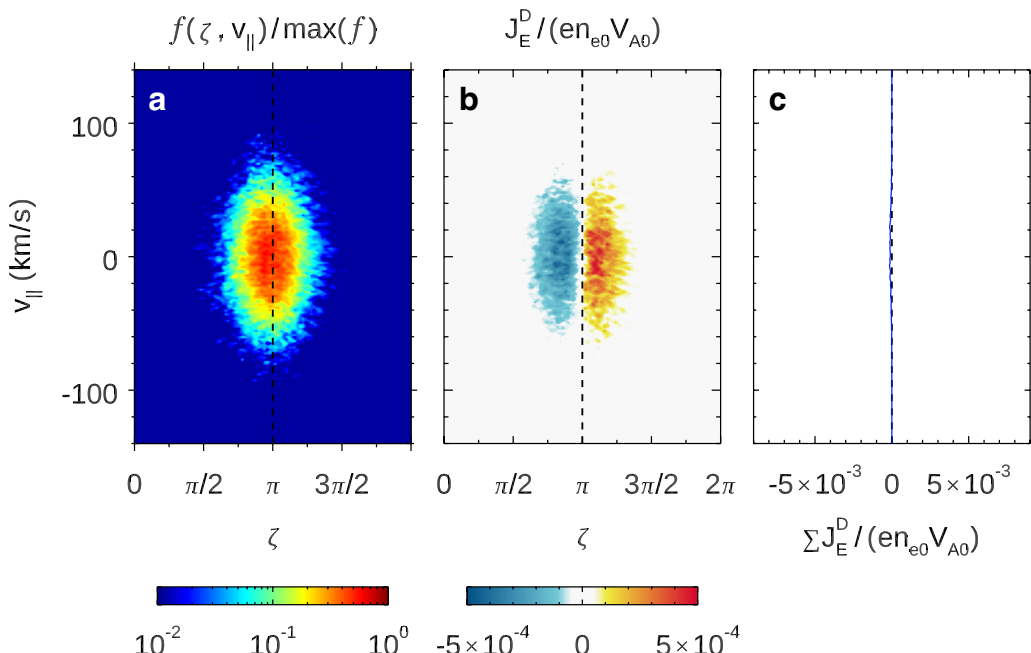


Fig. 11 Simulated phase space density of cold protons in the ζ - v_\parallel plane. **(a)** Normalized $f(\zeta, v_\parallel)$ and **(b)** differential resonant current J_E^D of cold protons at $t=18.7$ s. **(c)** The net integrated $\sum J_E^D$ as a function of v_\parallel . In panels **(a-b)**, the black dashed lines represent $\zeta=\pi$. In panel **(c)**, the black dashed line marks zero

waves), and zero indicating no energy transfer. Negative values of J_E^D appear at $\zeta < \pi$ and positive values at $\zeta > \pi$. However, since $f(\zeta, v_{||})$ is almost symmetric around $\zeta = \pi$, the integrated $\sum J_E^D$ over ζ is nearly zero (Fig. 11c), confirming no energy transfer in the nonresonant process. This agrees with the almost unchanged temperatures (Fig. 6a–b) and v_{\perp} (Fig. 9d), and can also be inferred from the $\mathbf{E} \times \mathbf{B}$ drift motion: the bulk flow velocity of cold protons is proportional to $\delta\mathbf{E} \times \hat{\mathbf{B}}_0$ (Fig. 6c–d; $\hat{\mathbf{B}}_0$ is the unit vector of \mathbf{B}_0), which is perpendicular to $\delta\mathbf{E}$ and thus contributes to null energy transfer. This conclusion also holds in the presence of a DC electric field, including convection electric fields (Matsui et al. 2003) and those in plasma sheet thinning regions (Hori et al. 2005), as the associated bulk velocity remains perpendicular to the electric field. In contrast, hot protons can transfer energy to waves (Chen et al. 2025). As illustrated in Fig. 10a, hot protons are phase-bunched with $-\delta\mathbf{E}$, resulting in negative J_E^D . Therefore, particle phase-bunching in stationary gyrophase is a necessary but not sufficient condition for identifying resonant interactions with waves. The energy transfer between waves and particles determines whether the response is nonresonant or resonant.

To simplify the plasma system, we perform a 1-D simulation to investigate the particle dynamics up to $\sim 15^\circ$. This is supported by observations showing that EMIC waves are predominantly quasi-parallel below $\sim 15^\circ$ (Min et al. 2012). The rising-tone chirping of EMIC waves (Fig. 3c) results from nonlinear interactions with hot protons (Omura et al. 2010) and has been investigated in a parallel work (Chen et al. 2025). In our simulation, the ion population consists only of protons, without He^+ or O^+ . The impact of heavy ions on wave excitation and their energization remain of interest for future work. In addition to EMIC waves, ULF waves can modulate the cold proton bulk flow through the $\mathbf{E} \times \mathbf{B}$ drift (Liu et al. 2022). Although Pc3 ULF waves are present in the simulation, the simulation duration is too short to analyze their effects.

5 Summary

Using MMS data and a hybrid simulation, we investigated the spatial and temporal evolution of cold proton dynamics in response to EMIC waves and distinguished the particle phase-bunching characteristics associated with nonresonant and resonant responses. The principal conclusions are as follows:

1. The energy flux of cold protons with $E_k < \sim 200$ eV increases due to their nonresonant response to EMIC waves, as the particle bulk flow is modulated by the wave electric fields. Despite the flux increase, the particle temperature remains nearly constant.

2. The flux enhancement of cold protons is more significant and extends to higher energy levels at higher magnetic latitudes.
3. The nonresonant response does not induce variations in particle number density; however, the number density exhibits spatial fluctuations near the magnetic equator due to nonlinear wave-wave coupling.
4. The phase-bunching distribution in stationary gyrophase results from either a nonresonant or resonant response. During the nonresonant process, particles are phase-bunched following $\varphi_{-\delta\mathbf{B}}$ due to $\mathbf{E} \times \mathbf{B}$ drift, with no energy exchange with waves. While during the resonant process, particles are phase-bunched following $\varphi_{-\delta\mathbf{E}}$, allowing energy transfer to waves. Therefore, particle phase-bunching is a necessary but not sufficient condition for identifying resonant interactions with waves.

Appendix A: Theoretical derivation of phase angle difference

The phase difference $\zeta = \pi$ between v_{\perp} of cold protons and $\delta\mathbf{B}$ of EMIC waves can be derived from the Lorentz force equation

$$\frac{d\mathbf{v}}{dt} = \frac{e}{m_p} [\delta\mathbf{E} + \mathbf{v} \times (\delta\mathbf{B} + \mathbf{B}_0)] \quad (7)$$

The electromagnetic fields $\delta\mathbf{B}$ and $\delta\mathbf{E}$ for forward-propagating EMIC waves are expressed as

$$\delta\mathbf{B} = \delta B e^{-i\theta} \quad (8)$$

$$\delta\mathbf{E} = \delta E e^{-i(\theta + \frac{\pi}{2})} \quad (9)$$

where i is the imaginary unit, and θ is the phase angle between $\delta\mathbf{B}$ and the $\mathbf{e}_{\perp 1}$ axis, with the clockwise direction defined as positive (see the sketch diagram in Fig. 12). The amplitudes δB and δE are assumed constant. We focus on the proton gyromotion by assuming the parallel velocity $v_{||} \sim 0$. The perpendicular velocity is given by

$$\mathbf{v}_{\perp} = v_{\perp} e^{-i\varphi} \quad (10)$$

where φ is the phase angle between v_{\perp} and $\mathbf{e}_{\perp 1}$. Equation (7) can be rewritten as

$$\frac{d\mathbf{v}_{\perp}}{dt} = \frac{e}{m_p} (\delta\mathbf{E} - iB_0\mathbf{v}_{\perp}) \quad (11)$$

or equivalently,

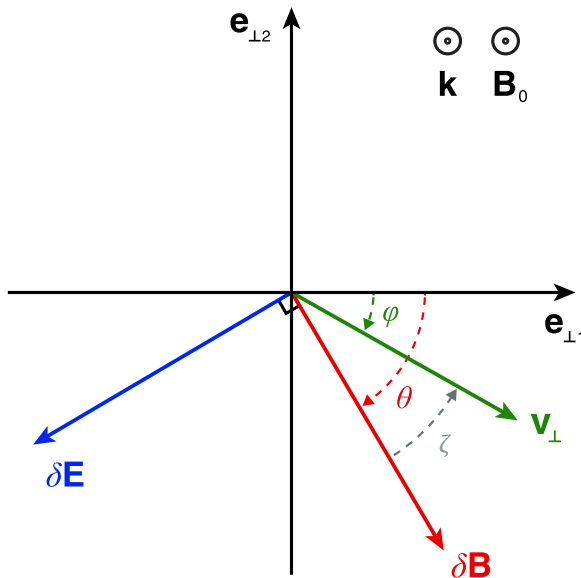


Fig. 12 Schematic diagram of electromagnetic fields in forward-propagating EMIC waves with $\mathbf{k} \cdot \mathbf{B}_0 > 0$. The unit vectors $\mathbf{e}_{\perp 1}$ and $\mathbf{e}_{\perp 2}$ define two perpendicular directions. The red and blue arrows indicate the wave magnetic field $\delta \mathbf{B}$ and electric field $\delta \mathbf{E}$, respectively, with the clockwise direction representing the positive phase angle θ . The green arrow indicates the proton perpendicular velocity \mathbf{v}_{\perp} with phase angle φ . The phase difference between \mathbf{v}_{\perp} and $\delta \mathbf{B}$ is ζ , with the counterclockwise direction defined as positive

$$\frac{d\mathbf{v}_{\perp}}{dt} + i\Omega_p \mathbf{v}_{\perp} = \frac{e}{m_p} \delta \mathbf{E} \quad (12)$$

Multiplying both sides of Equation (12) by $e^{i\Omega_p t}$ gives

$$e^{i\Omega_p t} \frac{d\mathbf{v}_{\perp}}{dt} + i\Omega_p e^{i\Omega_p t} \mathbf{v}_{\perp} = \frac{e}{m_p} e^{i\Omega_p t} \delta \mathbf{E} \quad (13)$$

Applying the Leibniz rule yields

$$\frac{d}{dt}(e^{i\Omega_p t} \mathbf{v}_{\perp}) = \frac{e}{m_p} e^{i\Omega_p t} \delta \mathbf{E} \quad (14)$$

For $\theta = -\omega t$, the integral form of Equation (14) becomes

$$e^{i\Omega_p t} \mathbf{v}_{\perp} = -\frac{e}{m_p(\Omega_p + \omega)} i \delta \mathbf{E} e^{i\Omega_p t} \quad (15)$$

Simplifying, we obtain

$$\mathbf{v}_{\perp} = \frac{e}{m_p(\Omega_p + \omega)} e^{-i\frac{\pi}{2}} \delta \mathbf{E} \quad (16)$$

Which gives

$$v_{\perp} = \frac{e}{m_p(\Omega_p + \omega)} \delta E \quad (17)$$

and

$$e^{-i\varphi} = e^{-i\frac{\pi}{2} - i(\theta + \frac{\pi}{2})} = e^{-i(\theta + \pi)} \quad (18)$$

Therefore,

$$\varphi - \theta = \pi \quad (19)$$

This result indicates that the phase difference between \mathbf{v}_{\perp} and $\delta \mathbf{B}$ is π , implying that cold protons are phase-bunched following the phase angle of $-\delta \mathbf{B}$, as shown in the phase space density in stationary gyrophase (Fig. 9a). Moreover, Equation (17) simplifies to $v = \delta E / B_0$ when $\omega \ll \Omega_p$, consistent with the drift velocity used in this study.

For backward-propagating EMIC waves (see Fig. 1f in Li et al. (2023)), if the phase of $\delta \mathbf{B}$ remains the same, the phase of $\delta \mathbf{E}$ shifts by π , resulting in

$$\delta \mathbf{E} = \delta E e^{-i(\theta - \frac{\pi}{2})} \quad (20)$$

Following Equation (16), the phase difference becomes

$$\varphi - \theta = 0 \quad (21)$$

indicating that cold protons are phase-bunched following the phase angle of $\delta \mathbf{B}$, resulting in $\zeta = 0$. This scenario is depicted in Fig. 3e and k in Li et al. (2023).

Acknowledgements

The authors thank the entire MMS team and instrument principal investigators for providing and calibrating data.

Author contributions

HC performed the simulations, processed the data, and prepared the manuscript. XW conceptualized the study, updated the simulation code, and revised the manuscript. LC and YO assisted with conceptualization. CW and HZ participated in manuscript revision. XL (Xiaolei Li) and YH optimized the computational algorithms. XL (Xinmin Li) processed the observational data. LA, HW, and NA provided the observational datasets.

Funding

This work was supported by NASA grants 80NSSC21K1688 and 80NSSC22K1012, and NSF grants AGS-2131012, AGS-2247759, AGS-2224109, and AGS-2453814. LC was supported by NSF grant AGS-2225121. CW was supported by NASA grant 80NSSC22K1012 and NSF-GEM 2224108. HZ was supported by NASA Grant 80NSSC24K1112. YO and YH were supported by JSPS KAKENHI Grant No.JP20H01960 and JP23H05429.

Data availability

The MMS observational data are available at <https://lasp.colorado.edu/mms/sdc/public/about/browse-wrapper/>. The simulation data are available from the corresponding author upon reasonable request.

Declarations

Ethics approval and consent to participate

Not applicable.

Consent for publication

Not applicable.

Competing interests

The author does not have any competing interests.

Author details

¹Department of Physics, Auburn University, Auburn, AL, USA. ²William B. Hanson Center for Space Sciences, University of Texas at Dallas, Richardson, TX, USA. ³Department of Atmospheric and Oceanic Sciences, University of California, Los Angeles, Los Angeles, CA, USA. ⁴Research Institute for Sustainable Humanosphere, Kyoto University, Kyoto, Japan. ⁵Boston University, Boston, MA, USA. ⁶NASA Goddard Space Flight Center, Greenbelt, MD, USA. ⁷Department of Earth, Planetary, and Space Physics, University of California, Los Angeles, CA, USA. ⁸Laboratory of Atmospheric and Space Physics, University of Colorado Boulder, Boulder, CO, USA.

Received: 12 October 2025 Accepted: 11 December 2025

References

- André M, Vaivads A, Khotyaintsev YV, Laitinen T, Nilsson H, Stenberg G, Fazakerley A, Trotignon JG (2010) Magnetic reconnection and cold plasma at the magnetopause. *Geophys Res Lett*. <https://doi.org/10.1029/2010GL044611>
- Asamura K, Shoji M, Miyoshi Y, Kasahara Y, Kasaba Y, Kumamoto A et al (2021) Cross-energy couplings from magnetosonic waves to electromagnetic ion cyclotron waves through cold ion heating inside the plasmasphere. *Phys Rev Lett* 127(24):245101. <https://doi.org/10.1103/PhysRevLett.127.245101>
- Axford WI (1968) The polar wind and the terrestrial helium budget. *J Geophys Res* 73(21):6855–6859. <https://doi.org/10.1029/JA073i021p06855>
- Berchem J, Gendrin R (1985) Nonresonant interaction of heavy ions with electromagnetic ion cyclotron waves. *J Geophys Res* 90(A11):10945–10960. <https://doi.org/10.1029/JA090iA11p10945>
- Carpenter DL, Anderson RR (1992) An ISEE & whistler model of equatorial electron density in the magnetosphere. *J Geophys Res* 97(A2):1097–1108. <https://doi.org/10.1029/91JA01548>
- Chen L, Bortnik J (2020) Chapter 4 - Wave-particle interactions with coherent magnetosonic waves. In: Jaynes AN, Usanova ME (eds) *The Dynamic Loss of Earth's Radiation Belts*. Elsevier, Amsterdam, <https://doi.org/10.1016/B978-0-12-813371-2.00004-4>
- Chen L, Thorne RM, Horne RB (2009) Simulation of EMIC wave excitation in a model magnetosphere including structured high-density plumes. *J Geophys Res*. <https://doi.org/10.1029/2009JA014204>
- Chen H, Gao X, Lu Q, Sun J, Wang S (2018a) Nonlinear evolution of counter-propagating whistler mode waves excited by anisotropic electrons within the equatorial source region: 1-D PIC simulations. *J Geophys Res Space Phys* 123:1200–1207. <https://doi.org/10.1002/2017JA024850>
- Chen H, Gao XL, Lu QM, Wang S (2018b) In situ observations of harmonic Alfvén waves and associated heavy ion heating. *Astrophys J* 859(2):120. <https://doi.org/10.3847/1538-4357/aaee2>
- Chen H, Gao X, Lu Q, Wang S (2019) Analyzing EMIC waves in the inner magnetosphere using long-term Van Allen Probes observations. *J Geophys Res Space Phys* 124:7402–7412. <https://doi.org/10.1029/2019JA026965>
- Chen H, Gao X, Lu Q, Tsurutani BT, Wang S (2020) Statistical evidence for EMIC wave excitation driven by substorm injection and enhanced solar wind pressure in the Earth's magnetosphere: two different EMIC wave sources. *Geophys Res Lett* 47:e2020GL090275. <https://doi.org/10.1029/2020GL090275>
- Chen H, Wang X, Chen L, Omura Y, Lu Q, Chen R et al (2023) Simulation of downward frequency chirping in the rising tone chorus element. *Geophys Res Lett* 50:e2023GL103160. <https://doi.org/10.1029/2023GL103160>
- Chen H, Wang X, Zhao H, Lin Y, Chen L, Omura Y et al (2024) Electron dynamics associated with advection and diffusion in self-consistent wave-particle interactions with oblique chorus waves. *Geophys Res Lett* 51:e2024GL110362. <https://doi.org/10.1029/2024GL110362>
- Chen H, Wang X, Lin Y, Zhao H, Wang C-P, Li X et al (2025) Nonlinear proton dynamics in the formation of rising-tone EMIC wave subpackets. *Geophys Res Lett* 52:e2025GL115834. <https://doi.org/10.1029/2025GL115834>
- Claudepierre SG, Toffoletto FR, Wiltberger M (2016) Global MHD modeling of resonant ULF waves: simulations with and without a plasmasphere. *J Geophys Res Space Phys* 121:227–244. <https://doi.org/10.1002/2015JA022048>
- de Soria-Santacruz M, Spasojevic M, Chen L (2013) EMIC waves growth and guiding in the presence of cold plasma density irregularities. *Geophys Res Lett* 40:1940–1944. <https://doi.org/10.1002/grl.50484>
- Delzanno GL, Borovsky JE, Henderson MG, Lira P, Roytershteyn V, Welling TD (2021) The impact of cold electrons and cold ions in magnetospheric physics. *J Atmos Solar-Terr Phys*. <https://doi.org/10.1016/j.jastp.2021.105599>
- Denton MH, Borovsky JE (2008) Superposed epoch analysis of high-speed-stream effects at geosynchronous orbit: hot plasma, cold plasma, and the solar wind. *J Geophys Res*. <https://doi.org/10.1029/2007JA012998>
- Denton RE, Menietti JD, Goldstein J, Young SL, Anderson RR (2004) Electron density in the magnetosphere. *J Geophys Res*. <https://doi.org/10.1029/2003JA010245>
- Denton RE, Jordanova VK, Fraser BJ (2014) Effect of spatial density variation and O⁺ concentration on the growth and evolution of electromagnetic ion cyclotron waves. *J Geophys Res Space Phys* 119:8372–8395. <https://doi.org/10.1002/2014JA020384>
- Engwall E, Eriksson A, Cully C et al (2009) Earth's ionospheric outflow dominated by hidden cold plasma. *Nat Geosci* 2:24–27. <https://doi.org/10.1038/ngeo387>
- Ergun RE, Tucker S, Westfall J, Goodrich KA, Malaspina DM, Summers D et al (2016) The axial double probe and fields signal processing for the MMS mission. *Space Sci Rev* 199:167–188. <https://doi.org/10.1007/s11214-014-0115-x>
- Gamayunov KV, Kim H, Shin Y (2024) EMIC wave energy dissipation as source of O⁺ conics and warm plasma cloak in the Earth's inner magnetosphere. *J Geophys Res Space Physics* 129:e2023JA032399. <https://doi.org/10.1029/2023JA032399>
- Gao XL, Lu QM, Wang SJ, Wang S (2018) Theoretical analysis on lower band cascade as a mechanism for multiband chorus in the Earth's magnetosphere. *AIP Adv* 8(5):055003. <https://doi.org/10.1063/1.5025507>
- Gary SP, Liu K, Chen L (2012) Alfvén-cyclotron instability with singly ionized helium: linear theory. *J Geophys Res* 117:A08201. <https://doi.org/10.1029/2012JA017740>
- Hori T, Lui ATY, Ohtani S, Brandt P, Mauk BH, McEntire RW, Maezawa K, Mukai T, Kasaba Y, Hayakawa H (2005) Storm-time convection electric field in the near-Earth plasma sheet. *J Geophys Res* 110:A04213. <https://doi.org/10.1029/2004JA010449>
- Horne RB, Thorne RM (1994) Convective instabilities of electromagnetic ion cyclotron waves in the outer magnetosphere. *J Geophys Res* 99(A9):17259–17273. <https://doi.org/10.1029/94JA01259>
- Hultqvist B (1971) On the production of a magnetic-field-aligned electric field by the interaction between the hot magnetospheric plasma and the cold ionosphere. *Planet Space Sci* 19(7):749–759. [https://doi.org/10.1016/0032-0633\(71\)90033-X](https://doi.org/10.1016/0032-0633(71)90033-X)
- Jacobs JA, Kato Y, Matsushita S, Troitskaya VA (1964) Classification of geomagnetic micropulsations. *J Geophys Res* 69(1):180–181. <https://doi.org/10.1029/JZ069i001p00180>
- Kang N, Lu Q, Gao X, Wang X, Chen H, Wang S (2021) Propagation of electromagnetic ion cyclotron waves in a dipole magnetic field: a 2-D hybrid simulation. *J Geophys Res Space Phys* 126:e2021JA029720. <https://doi.org/10.1029/2021JA029720>
- Kim K-H, Jun C-W, Kwon J-W, Lee J, Shiokawa K, Miyoshi Y et al (2024) Observation and numerical simulation of cold ions energized by EMIC waves. *J Geophys Res Space Physics* 129:e2023JA032361. <https://doi.org/10.1029/2023JA032361>
- Kitamura N, Kitahara M, Shoji M, Miyoshi Y, Hasegawa H, Nakamura S et al (2018) Direct measurements of two-way wave-particle energy transfer in a collisionless space plasma. *Science* 361(6406):1000–1003. <https://doi.org/10.1126/science.aap8730>
- Kwon J-W, Kim K-H, Jin H, Min K, Lee S-Y, Lee E (2023) Energization of cold protons and helium ions by EMIC waves in the inner magnetosphere: hybrid simulations. *J Geophys Res Space Phys* 128:e2022JA031240. <https://doi.org/10.1029/2022JA031240>
- Lee D-H, Hudson MK (2001) Numerical studies on the propagation of sudden impulses in the dipole magnetosphere. *J Geophys Res* 106(A5):8435–8445. <https://doi.org/10.1029/2000JA000271>
- Li J, Liu Z, Zhou X et al (2022) Anomalous resonance between low-energy particles and electromagnetic plasma waves. *Commun Phys* 5:300. <https://doi.org/10.1038/s42005-022-01083-y>

- Li X, Wang R, Gao X, Lu Q, Chen H, Ma J (2023) Observation of non-resonance interactions between cold protons and EMIC waves of different polarizations in the inner magnetosphere. *Geophys Res Lett* 50:e2023GL104431. <https://doi.org/10.1029/2023GL104431>
- Li J, Zhou X, Liu Z, Wang S, Artemyev AV, Omura Y, Zhang X, Li L, Yue C, Zong Q, Pollock C, Le G, Burch J (2024) Identification of coupled Landau and anomalous resonances in space plasmas. *Phys Rev Lett* 133:035201. <https://doi.org/10.1103/PhysRevLett.133.035201>
- Lindqvist PA, Olsson G, Torbert RB, King B, Granoff M, Rau D et al (2016) The spin-plane double probe electric field instrument for MMS. *Space Sci Rev* 199(1–4):137–165. <https://doi.org/10.1007/s11214-014-0116-9>
- Liu ZY, Tong QG, Rankin R et al (2022) Simultaneous macroscale and microscale wave-ion interaction in near-earth space plasmas. *Nat Commun* 13:5593. <https://doi.org/10.1038/s41467-022-33298-6>
- Lu QM, Li X (2007) Heating of ions by low-frequency Alfvén waves. *Phys Plasmas* 14(4):042303. <https://doi.org/10.1063/1.2715569>
- Matsui H, Mukai T, Ohtani S, Hayashi K, Elphic RC, Thomsen MF, Matsumoto H (1999) Cold dense plasma in the outer magnetosphere. *J Geophys Res* 104(A11):25077–25095. <https://doi.org/10.1029/1999JA900046>
- Matsui H, Quinn JM, Torbert RB, Jordanova VK, Baumjohann W, Puhl-Quinn PA, Paschmann G (2003) Electric field measurements in the inner magnetosphere by Cluster EDI. *J Geophys Res* 108:1352. <https://doi.org/10.1029/2003JA009913>
- Mauk BH (1982) Electromagnetic wave energization of heavy ions by the electric “phase bunching” process. *Geophys Res Lett* 9:1163–1166. <https://doi.org/10.1029/GL009i010p01163>
- Meredith NP, Horne RB, Sicard-Piet A, Boscher D, Yearly KH, Li W, Thorne RM (2012) Global model of lower band and upper band chorus from multiple satellite observations. *J Geophys Res* 117:A10225. <https://doi.org/10.1029/2012JA017978>
- Min K, Lee J, Keika K, Li W (2012) Global distribution of EMIC waves derived from THEMIS observations. *J Geophys Res* 117:A05219. <https://doi.org/10.1029/2012JA017515>
- Omidi N, Thorne R, Bortnik J (2010) Nonlinear evolution of EMIC waves in a uniform magnetic field: 1. hybrid simulations. *J Geophys Res* 115(A12):A12241. <https://doi.org/10.1029/2010JA015607>
- Omidi N, Bortnik J, Thorne R, Chen L (2013) Impact of cold O⁺ ions on the generation and evolution of EMIC waves. *J Geophys Res Space Phys* 118:434–445. <https://doi.org/10.1029/2012JA018319>
- Omura Y (2021) Nonlinear wave growth theory of whistler-mode chorus and hiss emissions in the magnetosphere. *Earth Planets Space* 73(1):95. <https://doi.org/10.1186/s40623-021-01380-w>
- Omura Y, Pickett J, Grison B, Santolik O, Dandouras I, Engebretson M, Décréau PM, Masson A (2010) Theory and observation of electromagnetic ion cyclotron triggered emissions in the magnetosphere. *J Geophys Res* 115:A07234. <https://doi.org/10.1029/2010JA015300>
- Pollock C, Moore T, Jacques A, Burch J, Gliese U, Saito Y et al (2016) Fast plasma investigation for magnetospheric multiscale. *Space Sci Rev* 199(1–4):331–406. <https://doi.org/10.1007/s11214-016-0245-4>
- Russell CT, Anderson BJ, Baumjohann W, Bromund KR, Dearborn D, Fischer D et al (2016) The magnetospheric multiscale magnetometers. *Space Sci Rev* 199(1–4):189–256. <https://doi.org/10.1007/s11214-014-0057-3>
- Shoji M, Miyoshi Y, Katoh Y, Keika K, Angelopoulos V, Kasahara S et al (2017) Ion hole formation and nonlinear generation of electromagnetic ion cyclotron waves: THEMIS observations. *Geophys Res Lett* 44(17):8730–8738. <https://doi.org/10.1002/2017GL074254>
- Summers D, Omura Y, Miyashita Y, Lee DH (2012) Nonlinear spatiotemporal evolution of whistler mode chorus waves in Earth’s inner magnetosphere. *J Geophys Res* 117:A09206. <https://doi.org/10.1029/2012ja017842>
- Wang X, Chen H, Omura Y, Hsieh Y-K, Chen L, Lin Y et al (2024) Resonant electron signatures in the formation of chorus wave subpackets. *Geophys Res Lett* 51:e2023GL108000. <https://doi.org/10.1029/2023GL108000>
- Young DT, Burch JL, Gomez RG, De Los Santos A, Miller GP, Wilson P et al (2016) Hot plasma composition analyzer for the magnetospheric multiscale mission. *Space Sci Rev* 199(1–4):407–470. <https://doi.org/10.1007/s11214-014-0119-6>
- Yue C, Jun C-W, Bortnik J, An X, Ma Q, Reeves GD et al (2019) The relationship between EMIC wave properties and proton distributions based on Van Allen probes observations. *Geophys Res Lett*. <https://doi.org/10.1029/2019GL082633>

Zhang H, Zhou K, Ge B-W, Guo Z-H, Tang B-B, Li W-Y et al (2025) Observations of two-layers spectrum formed by simultaneous H⁺ and He⁺ anomalous resonance with EMIC waves. *Geophys Res Lett* 52:e2025GL119563. <https://doi.org/10.1029/2025GL119563>

Publisher's Note

Springer Nature remains neutral with regard to jurisdictional claims in published maps and institutional affiliations.